ACCEPTED MANUSCRIPT

Accepted Manuscript

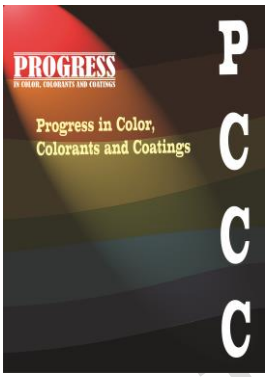

Title: Comparative Optimization and Electrochemical Assessment of Hydroxyapatite–Chitosan Composite Coatings on AISI 316L Stainless Steel Deposited by DC and Pulsed-DC Electrophoretic Deposition

Authors: Ayad Abbood Abdulhasan, Ewe Lay Sheng, Ali Mundher Mustafa, Mohd Rashdan Bin Isa

Manuscript number**: PCCC-2609-1543**

To appear in: Progresss in Color, Colorants and Coatings

Received: 17 September 2026

Final Revised: 15 November 2026

Accepted: 17 November 2026

Please cite this article as:

Ayad Abbood Abdulhasan, Ewe Lay Sheng, Ali Mundher Mustafa, Mohd Rashdan Bin Isa, Comparative Optimization and Electrochemical Assessment of Hydroxyapatite–Chitosan Composite Coatings on AISI 316L Stainless Steel Deposited by DC and Pulsed-DC Electrophoretic Deposition, Iran, Prog. Color, Colorants, Coat., 20 (2027) XX-XXX.
DOI: 10.30509/pccc.2026.167885.1543

This is a PDF file of the unedited manuscript that has been accepted for publication. The manuscript will undergo copyediting, typesetting, and review of the resulting proof before it is published in its final form

ACCEPTED MANUSCRIPT

Comparative Optimization and Electrochemical Assessment of Hydroxyapatite–Chitosan Composite Coatings on AISI 316L Stainless Steel Deposited by DC and Pulsed-DC Electrophoretic Deposition

A. Abbood Abdulhasan [1,2], E. Lay Sheng [1], A. Mundher Mustafa[3], M. Rashdan Bin Isa[1]

[1] Institute of Sustainable Energy (ISE), Universiti Tenaga Nasional (UNITEN), Putrajaya Campus, Jalan Kajang–Puchong, 43000 Kajang, Selangor, Malaysia.

[2] Department of Metallurgy Engineering, College of Engineering, Al-Mustafa University, 10064 Baghdad, Iraq.

[3] Department of Metallurgical Engineering, College of Production Engineering and Metallurgy, University of Technology–Iraq, 10001 Baghdad, Iraq.

Email: ayad.ce@almustafauniversity.edu.iq

Accepted Manuscript

Abstract

The investigation compares microstructural, adhesion-screening, and electrochemical responses of hydroxyapatite–chitosan composite coatings deposited on AISI 316L stainless steel using DC and pulsed DC electrophoretic deposition. A Taguchi L9 design evaluated voltage, deposition duration, nominal HA loading and prepared-substrate roughness. The greatest observed DC thickness was 23.25 µm (run 9: 60 V, 6 min, nominal HA level 3, Ra 0.05 µm); a separately reported confirmation value was 23.45 µm, although the confirmation settings require reconciliation with the laboratory record. From one exposed 10 × 10 mm face (1.00 cm²), the corrosion current densities were 1.8650×10^{-5}, 6.1900×10^{-7} and 1.1110×10^{-7} A/cm² for bare 316L, PDC–HA–chitosan and DC–HA–chitosan, respectively. The latter represents a 99.40% reduction compared with the uncoated control. ASTM G102-type uniform penetration rates calculated using assumed 316L equivalent weight and density are estimates rather than independently

ACCEPTED MANUSCRIPT

measured material-loss rates. The coatings are promising for corrosion mitigation; biological compatibility, clinical durability and unequivocal freedom from pitting are not established by the available measurements. This study evaluates hydroxyapatite–chitosan composite layers electrophoretically deposited on AISI 316L under DC and pulsed DC conditions. Thickness and morphology were evaluated using a Taguchi L9 design, and cross-cut observations and electrochemical polarization were compared. The maximum thickness observed in the DC L9 series was 23.25 μm. After normalizing corrosion currents to the measured exposed area of 1.00 cm², DC deposition gave the lowest i_corr (1.1110×10^{-7} A/cm²), representing a 99.40% reduction versus uncoated steel. A uniform-penetration estimate using assumed 316L alloy properties gave 0.001158 mm/year for DC, compared with 0.194391 mm/year for uncoated steel. Adhesion classification, porosity interpretation, diffraction-domain estimates and ANOVA inference are reported with their respective methodological limitations. No direct biological testing or service-life verification was conducted.

Keywords: Hydroxyapatite (HA), Direct Current (DC), Electrophoretic Deposition (EPD), Surface Roughness, Corrosion Resistance, Biomedical Coatings.

1. Introduction

Corrosion has a direct effect on how long medical implants last and how well they work with the body; therefore, it is very important to make biomedical coatings more resistant to corrosion and better adhere to surfaces. Implant materials that are in contact with complicated physiological environments lose their surface quality and ions, which could

ACCEPTED MANUSCRIPT

make them less useful over time [1, 2]. Hydroxyapatite (HA) coatings have demonstrated efficacy in improving the surface characteristics of metallic implants owing to their chemical resemblance to bone minerals, biocompatibility, osteoconductivity, and capacity to facilitate osseointegration [3-5]. HA creates a bioactive interface that improves implant fixation by allowing the bone and metal to bond directly [6].

AISI 316 L stainless steel is a popular biomaterial because it is strong, does not rust, and inexpensive [7, 8]. However, localized corrosion and ion release, especially of chromium and nickel, can lower its long-term performance and cause allergic or inflammatory reactions in vivo [9-11]. In chloride-rich environments, the electrochemical breakdown of 316 L accelerates pitting and shortens fatigue life [12, 13]. Consequently, the application of protective coatings to improve both biological and corrosion resistance has emerged as a principal area of research [14-16].

Scientists have developed a number of coating methods to fabricate bioactive surfaces, including electrophoretic deposition (EPD), sol–gel, plasma spraying, and magnetron sputtering [17, 18]. Among these, EPD stands out because it is easy to use, works at a low temperature, and can coat complex shapes with a uniform thickness [19]. In EPD, electrically charged particles in a stable colloidal suspension move toward a conductive substrate when an electric field is applied. This creates uniform ceramic or composite layers [20]. The final properties of the coating depend significantly on the voltage used, time it takes to deposit, concentration of particles, and type of current [21]. In continuous DC electrophoretic deposition, charged suspension species migrate toward the oppositely charged electrode. In PDC processing, intervening off periods permit partial relaxation of polarization and concentration gradients, potentially reducing gas-related defects; these

Accepted Manuscript

ACCEPTED MANUSCRIPT

mechanisms depend on pulse frequency, duty cycle and suspension conductivity. Because the pulse waveform is not fully documented, this mechanistic explanation is provisional rather than evidence for an experimentally established pulse–microstructure relationship.

The electrokinetic stability of the suspension, usually measured by the zeta potential (ζ), also affects the EPD performance. Higher ζ values indicate stronger electrostatic repulsion, which keeps particles from sticking together and makes coatings more uniform [2, 5, 9]. Chitosan, a naturally occurring cationic polymer, makes suspensions more stable and coatings stick better by creating electrostatic interactions and flexible networks that strengthen the material [2, 10]. Adding it to HA–polymer hybrids make the coating tougher, more biocompatible, and mildly antibacterial [11, 14].

Despite these benefits, it is still difficult for the brittle HA layer to adhere well to the metal substrate because their thermal expansion coefficients are not the same. Heat treatments after deposition (600-800 °C) can improve bonding and crystallinity but can also cause the substrate to oxidize, crack, and break down the HA phase [15, 17]. Consequently, creating room-temperature EPD methods that can make coatings that stick to surfaces, are crystalline, and do not corrode without sintering has become a major area of research [16, 18, 19].

The specific question addressed here is how the same nominal HA–chitosan suspension and four-factor Taguchi design respond to continuous and pulsed electrical excitation when applied to 316L stainless steel. The comparison evaluates deposition thickness, surface appearance, cross-cut retention, and normalized electrochemical response. Existing research has independently reported effects of suspension charge, ceramic loading and electric-field conditions on EPD coatings [13, 20, 21], but the present within-

ACCEPTED MANUSCRIPT

study comparison seeks to connect these responses under a common substrate and test framework. An assessment of experimental reproducibility and statistical uncertainty is limited by the available single-response records.

Systematic microstructural and electrochemical characterizations were performed to correlate the coating properties with the deposition conditions. AFM was used to quantify the nanoscale roughness, scanning electron microscopy (SEM) to analyze the morphology and homogeneity of the samples, and X-ray diffraction (XRD) determine the crystalline phases and purity of HA. Electrochemical testing, such as potentiodynamic polarization of simulated body fluid (SBF) and ion release by ICP-OES, yields valuable information regarding corrosion resistance and biocompatibility [7, 12, 20]. Optimized HA coatings were found to decrease ion release, improve corrosion resistance, and extend the lifespan of implants [6, 9, 13]. This contribution presents a consistent low-temperature method for preparing dense, adherent, and corrosion-resistant HA–chitosan coatings by coupling EPD optimization with extensive electrochemical and microstructural research.

The evaluation is restricted to the reported experimental conditions. In particular, the Taguchi ranking is descriptive without a replicated error estimate, and favorable corrosion polarization behavior should not be interpreted as proof of osseointegration, long-term biocompatibility, or immunity to localized corrosion.

2. Experimental

The experimental factor levels represented by the L9 table and the labeled cross-sectional specimens are 20, 40 and 60 V; deposition durations of 2, 4 and 6 min; nominal HA-

ACCEPTED MANUSCRIPT

loading levels of 1, 3 and 5; and pre-coating substrate roughness Ra of 0.05, 0.03 and 0.01 µm. All thickness comparisons and response summaries in this work use these recorded L9 levels. The isolated earlier narrative referring to 1, 3 and 5 min has been corrected to correspond to the actual tabulated series.

The deposited system is designated HA–chitosan composite throughout because the suspension incorporated chitosan as a dispersing and binding constituent. HA concentrations are treated as the nominal formulation levels 1, 3 and 5 used to label the experimental runs. The accompanying source records contain both g/L and percentage conventions; therefore the analysis does not impose an unsupported gravimetric wt% conversion.

Commercial-grade AISI 316 L stainless steel was chosen as the metallic substrate because it is strong and does not rust. A precision water-jet machine was used to cut out rectangular plates with dimensions of 10 mm (length) × 10 mm (width) × 5 mm (thickness), equivalent to 1.0 × 1.0 × 0.5 cm. The composition was found to be 0.033% C, 0.31% Si, 1.55% Mn, 16.50% Cr, 2.02% Mo, 9.7% Ni, 0.0028% Al, 0.165% Co, 0.46% Cu, 66.3% Fe, 0.0259% P, and 0.024% S.

hydroxyapatite (HA, 99% purity, 25–90 nm, 3.19 g/cm³) from Sigma-Aldrich (USA) and chitosan (Chit, 30–80 µm, ~85% deacetylation, medium molecular weight) powders. Chitosan was both a dispersing and binding agent because it dissolved in 1% acetic acid. Analytical-grade ethanol (99.9%) and acetic acid (98%) were used as the solvents without further purification. Deionized water was used in all preparations.

The substrates were finished using 600-, 800- and 1000-grit SiC paper. The reported profilometric roughness descriptor is Ra, with corresponding recorded values of 0.05,

ACCEPTED MANUSCRIPT

0.03 and 0.01 μm. Abrasive grit is treated as a preparation condition and is not mathematically equated to roughness. The comparison concerns the documented Ra groups and does not incorporate unreported within-group standard deviations or directional roughness effects.

The HA–chitosan suspension was formulated in an ethanol–water mixture with acetic acid to facilitate chitosan dissolution. The related experimental record describes 95 mL ethanol and 5 mL deionized water for a nominal 100 mL solvent batch and a chitosan concentration of 0.05 g per 100 mL, corresponding to 0.5 g/L. The HA factor was recorded at nominal loading levels 1, 3 and 5. These nominal levels are preserved in the experimental matrix and analysis rather than being converted into an unsubstantiated wt% definition. The suspension was magnetically stirred for 6 h and ultrasonicated for 30 min before EPD.

A Malvern Nano ZS analyzer was used to calculate the zeta potential and electrophoretic mobility. In the case of the 1, 3, and 5 percent HA suspensions, ζ = +24.06, +45.09 and +31.00 mV, respectively. This indicates that colloidal stability was maintained.

Two 316L plate electrodes separated by 10 mm were used for deposition near room temperature. Applied potentials were 20, 40 and 60 V and deposition durations were 2, 4 and 6 min according to the actual nine-run tables. DC and pulsed DC were examined separately. Pulse duty cycle, frequency and actual time-resolved current data were not included among the supplied records and must not be retrospectively assumed. The coated samples were air-dried after deposition without a reported sintering step. Four three-level control factors were organized into an L9 orthogonal design. For one thickness observation t per experimental run, the larger-the-better signal-to-noise

Accepted Manuscript

ACCEPTED MANUSCRIPT

transformation is S/N = 20 log10 (t/1 μm). This expression was applied to all reported individual thickness values, including the corrected PDC run 9. Here S/N is a descriptive logarithmic response for each single observation; it does not independently estimate variation between replicates.

For each current mode, the four three-level factors consume 4 × (3–1) = 8 degrees of freedom, equal to the total degrees of freedom of the unreplicated nine-run design. Thus the residual error has zero degrees of freedom, so statistically valid F tests, p values, confidence intervals and declarations of factor "significance" cannot be obtained from this saturated model without independent error estimates or justified pooling assumptions. The reported ANOVA contributions are interpreted solely as descriptive shares of the observed response variation, not inferential statistical significance.

Coating morphology was assessed by optical microscopy, SEM and AFM, and phase indications were considered from the reported XRD patterns. Cross-cut testing according to ASTM D3359 Method B was used as a qualitative coating-retention screen, not a quantitative bond-strength measurement. Electrochemical responses were acquired by polarization in simulated body fluid at 37 ± 1 °C. A single 10 × 10 mm front face was exposed to the electrolyte during each corrosion measurement; the remaining faces and edges were masked, fixing the wetted area at 1.00 cm². Corrosion currents were divided by this exposed area to obtain current densities. Chromium release reported after immersion in 0.9% NaCl represents a different test medium and is discussed separately. The entire process involved preparing the substrate, making the suspension, performing EPD in both DC and PDC modes, drying, and fully characterizing the product. Combining Taguchi optimization and ANOVA with microstructural and electrochemical

ACCEPTED MANUSCRIPT

evaluations ensured that the process parameters were measured in a way that was both quantitative and repeatable. This low-temperature method is a long-lasting and energy-efficient way to fabricate HA–chitosan coatings that adhere to 316 L stainless steel and are resistant to corrosion.

Table 1. L9 Orthogonal Array of variables and the corresponding levels for HA layer deposition

Experiment No.	Voltage (V)	Deposition Time (min)	HA Concentration (% wt)	Surface Roughness (µm)
1	20	2	1	0.05
2	20	4	3	0.03
3	20	6	5	0.01
4	40	2	3	0.01
5	40	4	5	0.05
6	40	6	1	0.03
7	60	2	5	0.03
8	60	4	1	0.01
9	60	6	3	0.05

3. Results and Discussions

3.1. Solution stability

Suspension characterization: Positive measured zeta potentials of +24.06, +45.09 and +31.00 mV for the three nominal HA levels indicate differences in electrokinetic behavior; the largest magnitude is observed at the middle level. Zeta potential alone does not establish long-term colloidal stability, layer bioactivity, or biological safety.

The stability of the electrophoretic suspension, which is based on the balance between electrostatic repulsion and van der Waals attraction among particles, controlled the homogeneity, packing density, and adhesion of the HA–chitosan coatings. Table 2 shows the results of zeta potential (ζ) measurements, which are important for colloidal stability [14, 15]. The measured ζ values of +24.06, +45.09, and +31.00 mV for 1%, 3%, and 5%

ACCEPTED MANUSCRIPT

HA concentrations, respectively, showed that the dispersions were moderately to very stable, with the 3% HA showing the best stability. Table 1 shows the distribution of electrokinetic potentials. This shows that the 3% HA suspension was in the ideal ζ-potential window (+30 to +50 mV). At this concentration, a thick electric double layer (EDL) formed when the negatively charged phosphate groups (PO_4^{3-}) of HA and the positively charged amine groups ($–NH_4^+$) of chitosan interacted with each other through electrostatic forces. This strong repulsive energy barrier prevents particles from sticking together and settling down, which allows the HA–chitosan complexes to move smoothly under an electric field to form a uniform coating [18].

However, the 1% HA suspensions were unstable because there were not enough particles to cause interparticle repulsion. The 5% HA suspensions had a lower ζ-potential and some flocculation, because there were too many solids and collisions. Prior research has indicated that optimal EPD film formation transpires at ζ-potentials ranging from +30 to +50 mV [19]. Therefore, the 3% HA suspension provided the best coating environment, which was stable, compact, and free of cracks (Table 2).

Table 2. Examination of the mobility and zeta potential dynamics

Suspensions	Zeta potential (mv)	mobility
1% HA	24.06	2.38
3% HA	۴۵.۰۹	۳/۴۵
5% HA	31.00	3.06

3.2. Thickness determent for HA coating layer by using DC

During direct current (DC) electrophoretic deposition (Table 3), there was a strong link between the voltage used, time taken to deposit, roughness of the surface, and thickness

ACCEPTED MANUSCRIPT

of the coating. The coating thickness increased in a straight line with a voltage of up to 60 V, reaching a maximum of 23 μm. Subsequently, no noticeable change was observed. Hamaker's law ($m = C \cdot \mu \cdot E \cdot t$) states that the mass deposited (m) is directly related to the electric field strength (E), electrophoretic mobility (μ), and time it takes to deposit (t).

Coating thickness depends on field-driven electrophoretic transport, deposition duration, suspension properties and interfacial conditions. Hamaker-type models describe an ideal early-stage mass-deposition tendency, but measured thickness in this L9 design is not monotonic in voltage or time because composition and roughness vary between runs. It is therefore not valid to attribute the maximum thickness to a single parameter without considering the other assigned factors.

The surface roughness factor showed the largest descriptive contribution in the DC L9 response decomposition (65.12%). This finding is consistent with a possible contribution of surface topography to deposition and retention, but the lack of replicated measurements and a residual error estimate precludes a significance test or an isolated causal mechanism.

The greatest observed thickness in the nine DC runs was 23.25 μm for run 9 (60 V, 6 min, HA level 3 and Ra = 0.05 μm), with S/N = 27.3285 dB. The separately reported 23.45 μm value is described as an additional reported thickness and not conflated with a 2 min experiment. The measured maximum within the L9 array is thus distinguished from any main-effect optimum inferred from factor-level averages. The comparison of the nine tested combinations uses the directly reported responses.

In general, The DC–HA coating exhibited a dense and compact structure, more uniform in its internal morphology than the PDC counterpart. Figure 1 shows a cross-section of

Accepted Manuscript

ACCEPTED MANUSCRIPT

sample No. 1, which shows that the coating is even and sticks well to the stainless-steel substrate.

Table 3. Signal-to-noise ratio of the Taguchi design of (L9) for the thickness of the HA coating layer using DC

NO.	V	T, min	C %	S. R	Thickness µ m	SNRA1	MEAN1
1	20	2	1	0.05	16.73	24.4699	16.73
2	20	4	3	0.03	13.15	22.3785	13.15
3	20	6	5	0.01	10.36	20.3072	10.36
4	40	2	3	0.01	16.94	24.5783	16.94
5	40	4	5	0.05	18.62	25.3996	18.62
6	40	6	1	0.03	11.57	21.2667	11.57
7	60	2	5	0.03	11.86	21.4817	11.86
8	60	4	1	0.01	14.95	23.4928	14.95
9	60	6	3	0.05	23.25	27.3285	23.25

Table 4: Rank of using direct current (DC) to modify thickness-controlling parameters in HA layer

Level	V	t	C%	S. R
1	22.39	23.51	23.08	22.79
2	23.75	23.76	24.76	21.71
3	24.10	22.97	22.40	25.73
Delta	1.72	0.79	2.37	4.02
Rank	3	4	2	1

ACCEPTED MANUSCRIPT

ACCEPTED MANUSCRIPT

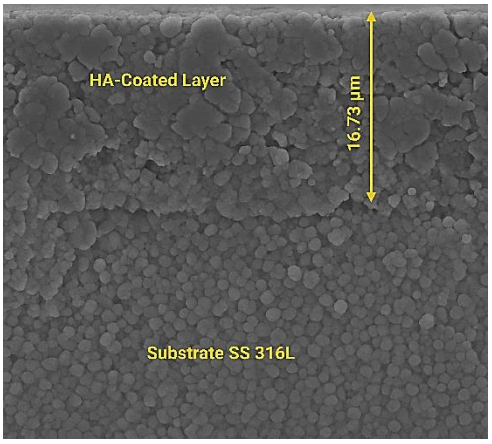

Figure 1. Sideview of the DC-HA coating layer for sample no.1

Table 5. DC modeling-based statistical analysis (ANOVA) of the HA layer thickness.

Variable	DF	Sum of squares SS	Adj MS	R-Sq
V	2	16.943	8.4716	12.66
T	2	0.434	0.2172	0.32
C%	2	29.318	14.6592	21.90
S. R	2	87.150	43.5751	65.12
Errors	0	-	-	-
Total	8	133.846	-	100.00

Because the nine DC runs include four factors with two degrees of freedom each, the ANOVA model exhausts all eight degrees of freedom and has no residual error degrees of freedom. Accordingly, the reported factor contributions (roughness 65.12%, nominal HA level 21.90%, voltage 12.66%, time 0.32%) are descriptive partitions only. Neither the original model nor a hypothetical pooled-error model demonstrates statistically significant effects unless its error assumptions and any replication are documented. This limitation should be considered when interpreting the ranking and selecting a follow-up confirmation experiment.

Accepted Manuscript

ACCEPTED MANUSCRIPT

3.3. Thickness determination of HA coating layer using DC Pulses

Pulsed-DC deposition gave recorded thicknesses between 10.86 and 15.76 μm in the nine-run series. The largest observed value, 15.76 μm, occurs in experiment 9 (60 V, 6 min, nominal HA level 3, Ra 0.05 μm), not at the previously asserted 20 V, 2 min and nominal HA level 5 setting. The latter may have been suggested by a separate selection criterion, but no verifiable multiresponse confirmation for that condition was supplied. The observed PDC thicknesses are lower than the largest DC thickness, although direct attribution to pulse relaxation is limited by the unavailable waveform settings.

Using S/N = 20 log10(t/1 μm) for the nine single thickness observations, corrected PDC values for runs 1–9 are 20.8041, 23.8402, 21.8333, 23.8010, 20.7166, 23.8346, 21.9173, 21.0462 and 23.9511 dB, respectively. Run 9 has thickness 15.76 μm and the highest observed PDC response. These entries are internally consistent transformations of the documented measurements rather than replicate-based estimates of experimental variability.

Even though they grew more slowly, the PDC coatings had smoother, more even shapes, and much lower internal stresses. The intermittent current enabled ionic diffusion equilibrium and stress relaxation during the OFF cycles, improving the coating flexibility and overall film integrity [21]. Figure 2 shows SEM micrographs that compare the shapes of HA–chitosan coatings made in the DC and PDC modes.

Image A (DC–HA coating): A microstructure that is dense and uniform, with HA grains that are almost spherical with an average size of 120 nm, and small agglomerates of approximately 520 nm in size. The compact and well-adhered layer showed that the electrophoretic mobility was stable, the particles were evenly spread out, and the layer

ACCEPTED MANUSCRIPT

was strongly bonded to the stainless-steel substrate. Image B (PDC–HA coating): You can see bigger agglomerates (about 590 nm) and pores that are between 3.2 and 5.1 μm wide. This is because the flow of the particles stopped during OFF times. The coating surface appeared smoother and had fewer microcracks because there was less residual and thermal stress, even though it was less dense. In general, The PDC–HA coating produced a smoother surface morphology, although its structural compactness was slightly lower than that of the DC–HA layer.

Table 6. Signal-to-noise ratio of Taguchi design of (L9) for the thickness of the HA coating layer using DC pulses.

NO.	V	T, min	C %	S. R	Thickness (μ m)	SNRA1	MEAN1
1	20	2	1	0.05	10.97	20.8041	10.97
2	20	4	3	0.03	15.56	23.8402	15.56
3	20	6	5	0.01	12.35	21.8333	12.35
4	40	2	3	0.01	15.49	23.8010	15.49
5	40	4	5	0.05	10.86	20.7166	10.86
6	40	6	1	0.03	15.55	23.8346	15.55
7	60	2	5	0.03	12.47	21.9173	12.47
8	60	4	1	0.01	11.28	21.0462	11.28
9	60	6	3	0.05	15.76	23.9511	15.76

All nine PDC S/N entries were corrected using the individual recorded thicknesses and the equation S/N = 20 log10(t/1 μm). For experiment 9, t = 15.76 μm and S/N = 23.9511 dB; the copied run-1 entries have been eliminated. In this L9 series, run 9 at 60 V, 6 min, HA level 3 and Ra = 0.05 μm was the highest measured PDC-thickness combination. The former assertion that 20 V and 2 min was the highest observed setting has been removed.

Accepted Manuscript

ACCEPTED MANUSCRIPT

Table 7. Ranking of using direct current (DC) pulses to modify thickness-controlling parameters in the HA layer

Level	V	t	C%	S. R
1	23.37	23.71	22.69	22.53
2	22.12	22.17	21.23	21.79
3	22.27	21.87	23.83	23.43
Delta	1.25	1.84	2.60	1.65
Rank	4	2	1	3

The analysis showed that the HA concentration had the most significant influence (Δ = 2.60; rank 1), followed by the deposition time (Δ = 1.84; rank 2), surface roughness (rank 3), and voltage (rank 4). This trend indicates that particle loading and deposition duration control the compaction and growth rate of the coating.

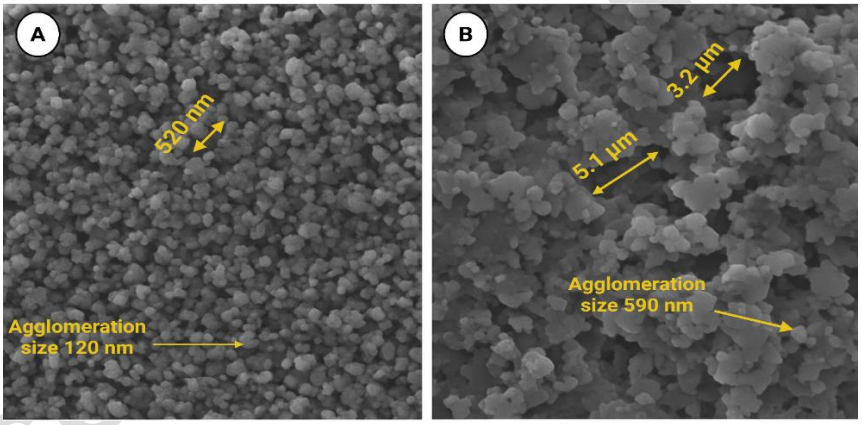

Figure 2 SEM micrographs comparing HA–chitosan coatings: (A) DC deposition showing a dense and strongly adhered layer with fine grains (~120 nm) and uniform distribution; (B) PDC deposition showing smoother surface morphology, larger agglomerates (~590 nm), and micro voids (3.2–5.1 µm) due to pulsed current cycles.

For the PDC design, all eight available degrees of freedom are allocated to four three-level factors. Factor contributions derived from sums of squares are therefore used descriptively, without assigning F values or p values. The originally reported percentages (40.72% HA level, 25.99% duration, 18.70% roughness and 14.59% voltage) are identified as the original decomposition, not as independently validated significance

ACCEPTED MANUSCRIPT

estimates after the corrected response entries.

Table 8. The HA layer thicknesses were statistically analyzed (ANOVA) using DC pulse modelling.

Variable	D F	Sum of squares SS	Variance MS	R-Sq
V	2	3.385	4.384	14.59
T	2	2.558	7.808	25.99
C%	2	11.253	12.237	40.72
D	2	7.351	5.619	18.70
Errors	0	-	-	-
Total	8	24.546	-	100.00

As for DC, the saturated PDC L9 permits a descriptive comparison of the tested conditions and main effects but no internally estimated residual error. Coating uniformity is discussed using the observed surface images, separately from the thickness-only S/N transformation.

3.4. Evaluation of adhesion and surface morphology of HA coatings

The reported apparent pore fractions describe distinct observation scales rather than interchangeable volumetric porosities. The value near 1.25% was obtained from thresholded AFM surface mapping, whereas approximately 7.9% for DC and 8.2% for PDC came from image segmentation of SEM micrographs. All are method- and threshold-dependent two-dimensional image-area fractions. They cannot establish three-dimensional open porosity, connected-fluid pathways, or bulk void volume without complementary stereology or porosimetry.

The reported cross-cut image area removal of 6.8% for DC and 17% for PDC corresponds to ASTM D3359 Method B ordinal ratings of 3B (5–15% affected) and 2B

ACCEPTED MANUSCRIPT

(15–35% affected), respectively, assuming that the counted area meets the standard's grid-intersection criteria. These classes provide comparative tape-test retention only; neither yields adhesion stress in MPa or establishes suitability for a load-bearing implant. Quantitative tests such as appropriate tensile/bond or scratch procedures are needed to investigate service-relevant interfacial strength.

The cross-cut tape observations favor DC coating retention over PDC under the stated evaluation conditions (6.8% versus 17% affected area). After correct ASTM D3359 classification, the samples are rated 3B and 2B, respectively, rather than 5B and 3B. The results suggest different coating integrity under adhesive tape removal but do not constitute a direct measurement of tensile or shear adhesion strength.The cross-cut test produced a reported affected area of 6.8% for DC and 17% for PDC; using ASTM D3359 Method B these correspond approximately to ratings 3B and 2B, respectively, provided the affected areas were scored in accordance with the standard. Thus DC displayed better comparative retention, but the data cannot be converted to adhesive bond stress and should not be described as 5B or as a direct assessment of load-bearing suitability.

SEM images suggest a comparatively compact DC deposit and a more visibly aggregated PDC structure. AFM surface roughness values reported for these selected surfaces are approximately 58 nm (DC) and 36 nm (PDC), which represent post-coating topography and should not be confused with the initial substrate Ra levels of 0.01–0.05 µm. The associated SEM apparent pore-area fractions of approximately 7.9% and 8.2% differ slightly; their difference should not be assigned statistical significance without replicated image fields and threshold-sensitivity analysis.

The much lower 1.25% thresholded AFM surface feature fraction is not a direct

ACCEPTED MANUSCRIPT

contradiction of the SEM-based values, because imaging resolution, sampling depth, segmentation and feature definition differ. However, neither dataset documents a volumetric porosity of the full coating; quantitative comparisons across these two methods should be avoided.

The thresholded SEM images yield apparent two-dimensional feature-area fractions, not three-dimensional porosity or a statistical distribution of all pore sizes. The quoted values are therefore retained as image-based descriptors, with interpretation directed to the observed larger interparticle gaps and the relative coating continuity visible in the images. Consequently, the different apparent pore fractions should be discussed as scale-specific image descriptors rather than proof of a hierarchical three-dimensional pore structure. The DC images are qualitatively compatible with a more continuous barrier, a hypothesis supported independently by the lower normalized corrosion current. Although surface morphology may affect electrolyte penetration and coating retention, the micrographs alone cannot establish the pore connectivity or diffusion rate. The observed electrochemical differences therefore support, but do not directly prove, a defect-mediated barrier mechanism.

These agree with findings by Gopi et al. [21] and Azar et al. [19], who stated that continuity of the DC field enhances cohesion and prevents microcrack formation. Abed et al. [16] and Hlinka et al. [11] also found that under appropriate conditions, dense and homogenous microstructures result in more interfacial strength due to minimization of interfaces and discontinuities. Fosca et al. [13] also reported that chemical bonds such as Ca-O-O-Fe-PO_4 at the interface contribute to adhesion of the two surfaces and stability in time of the coating.

Accepted Manuscript

ACCEPTED MANUSCRIPT

Within the tested conditions, DC deposition yielded better comparative cross-cut retention and a lower normalized electrochemical corrosion current than PDC deposition. These findings substantiate a relative protective performance of the coatings under the reported laboratory test conditions, without representing direct measurements of implant service lifetime or biological tissue response.A smoother PDC AFM topography (Ra ≈ 36 nm versus 58 nm for DC) does not necessarily imply better cross-cut retention or lower corrosion current. Nanoscale height variation, interface anchoring, film continuity and electrolyte-accessible defects describe different physical attributes. Thus the observed retention and corrosion advantage of the DC coating is not incompatible with a smoother measured PDC surface.

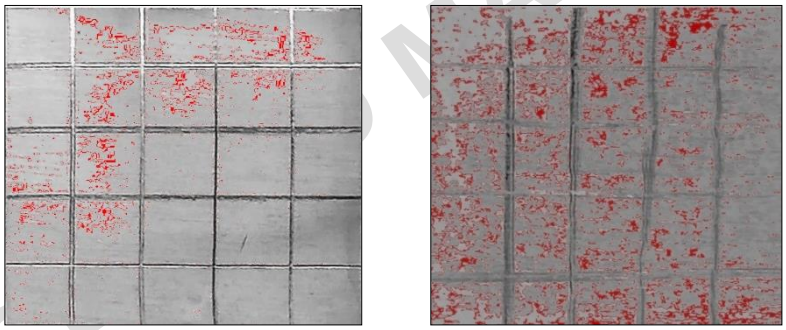

Figure 3. Optical images of the deposited HA coating. (1) The removal area ratio of the coated layer DC-HA was 6.8%. (2) Removal area ratio of the coated layer DC Pulses-HA 17%.

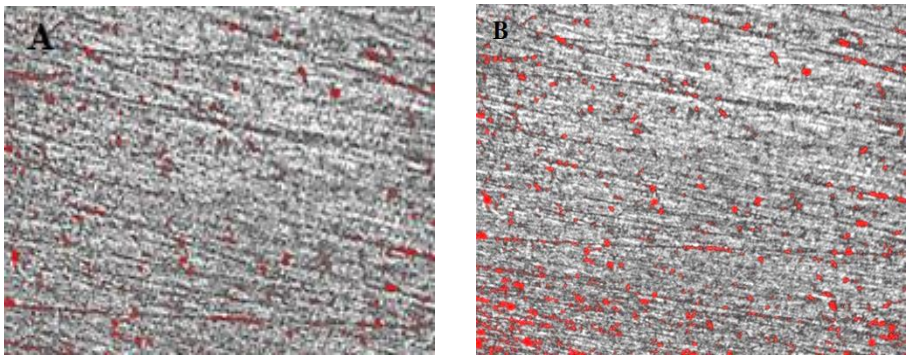

Figure 4. Porosity estimation for a single (a)DC-HA layer(b) DC pulse-HA

ACCEPTED MANUSCRIPT

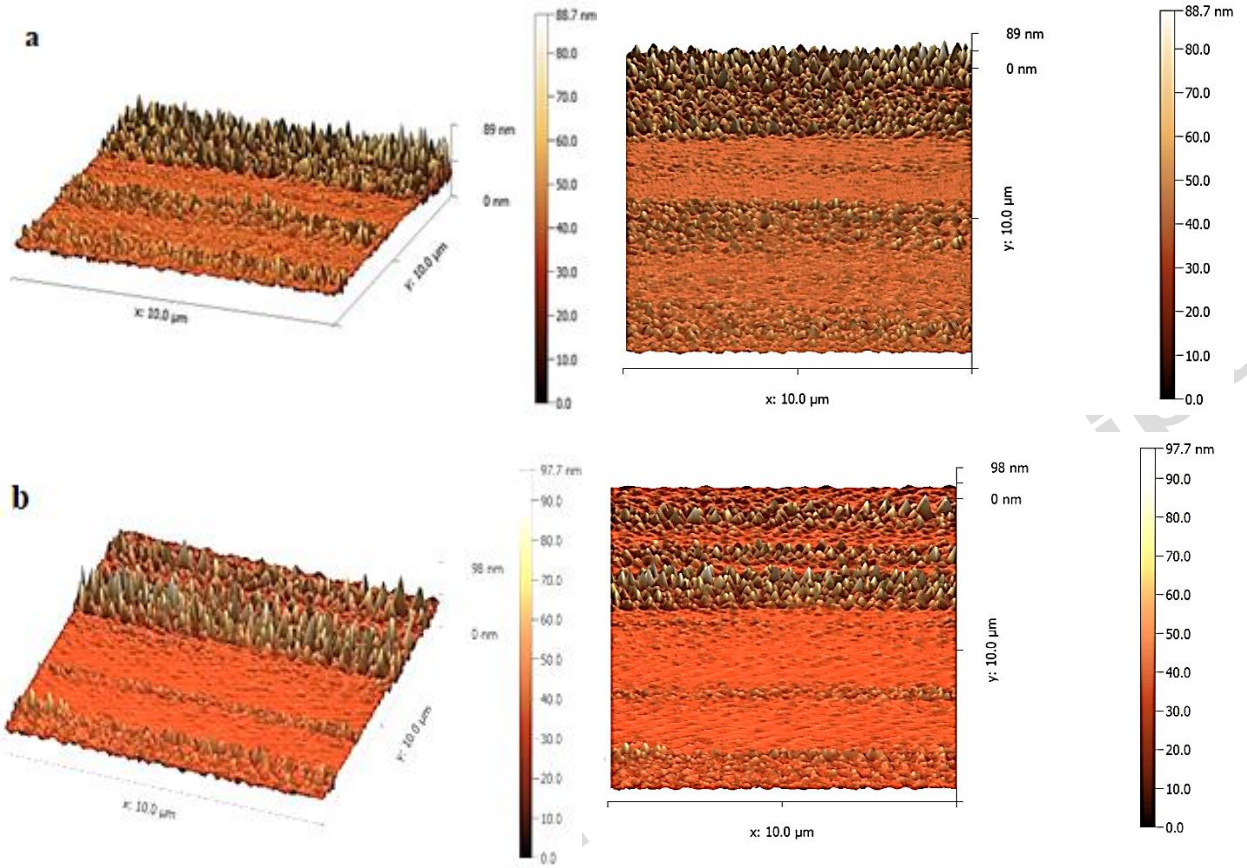

Figure 5. (AFM) images for the optimal parameters for(a) DC-HA layer (b) DC Pulses-HA.

3.5. XRD analysis results

The 21.9 nm figure is reported as an apparent Scherrer coherent diffraction-domain size, and is not equivalent to an SEM-visible particle diameter. The approximately 120 nm primary surface features and 520-590 nm agglomerates are larger because each particle or cluster may contain multiple coherently diffracting domains. The original XRD intensity-versus-angle dataset, instrumental line broadening, peak FWHM, fitted peak position and instrument-standard measurements were not provided; accordingly the numerical 21.9 nm estimate cannot be independently verified and should be regarded as provisional. Figure 6 presents reported X-ray diffraction traces for uncoated AISI 316L and HA–chitosan-

ACCEPTED MANUSCRIPT

coated specimens. The interpretation uses the cited austenitic stainless-steel reference (33-0397) and HA reference (09-0432). Coated-sample reflections are consistent with crystalline HA, although overlap with substrate peaks restricts the certainty of minor-phase exclusion. For the reported 21.9 nm crystallite-size figure, the Scherrer relation is $D = K\lambda/(\beta \cos \theta)$, where β is the instrument-corrected full width at half maximum in radians. As no quantitative peak-fit results accompany the plotted figure, 21.9 nm is treated as the reported approximate coherent-domain size, not a new independently calculated value.

The strongest austenitic 316L reflections are associated with the (111), (200) and (220) families. Hydroxyapatite gives multiple reflections, including a feature near 25.9° and closely spaced reflections near 31-33° (2θ, Cu $K\alpha$), with overlap and substrate contributions in the remaining pattern. The phase assignment is therefore expressed as "consistent with crystalline HA" rather than an unqualified proof of complete phase purity. This wording matches the resolution of the diffraction traces reproduced in Figure 6.

Peak-width differences between the displayed DC and PDC profiles may result from crystallite size, microstrain, texture, background and instrument broadening. Without extracted FWHM values and instrument corrections, it is not possible to assign a smaller coherent-domain size to PDC or a higher crystallinity to DC quantitatively. A Ca/P atomic ratio close to 1.67, where available, is a compositional indicator and does not independently prove biological performance.

Taken together, the XRD and SEM images indicate retention of HA-related diffraction features and microstructural assembly into larger surface clusters. These observations are

ACCEPTED MANUSCRIPT

compatible with the electrochemical advantage of DC but do not, by themselves, quantify crystalline domain size, coating phase purity, adhesion stress, or osseointegration.

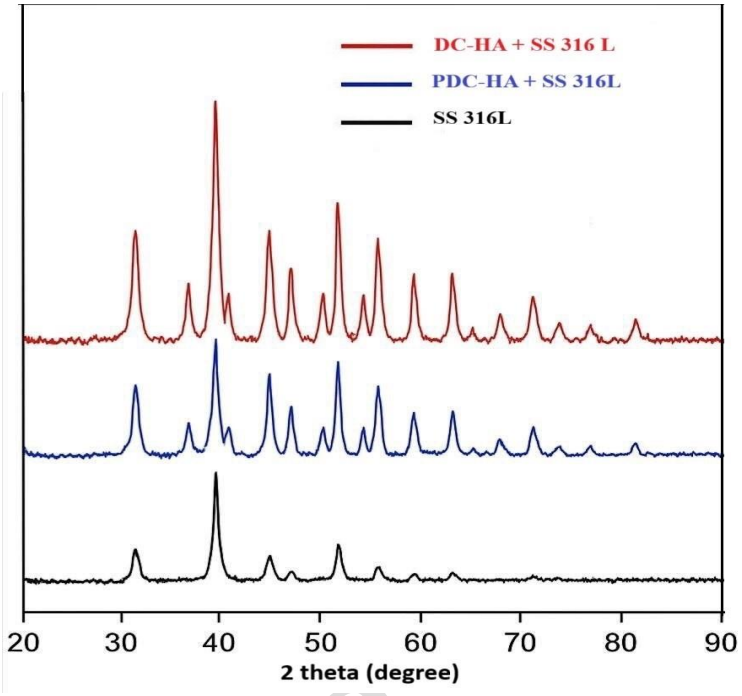

Figure 6. XRD for SS 316L and with DC-HA and PDC-HA.

3.6. Corrosion behavior of S.S 316 L and HA coatings.

The corrosion potential Ecorr and pitting potential Epit are different observables: Ecorr is obtained from the mixed-potential/Tafel region, whereas Epit denotes the onset of sustained breakdown during an anodic scan under a defined protocol. Previously quoted positive Epit values cannot replace or be compared directly with negative Ecorr values in Table 9. The original data do not supply an independently verifiable set of breakdown and repassivation potentials; therefore no definitive “no pitting” claim is made for the DC-coated sample.

The electrochemical assessment combined polarization testing in simulated body fluid (SBF) with separate chromium release measurements following immersion in 0.9% NaCl.

ACCEPTED MANUSCRIPT

The corrosion potentials and current-derived metrics are evaluated from the polarization data; the Cr release observations provide supporting chemical evidence under a different medium and timescale. The reported chromium concentrations after immersion were 0.00702 ppm for uncoated steel, 0.00291 ppm for PDC-coated steel and 0.00138 ppm for DC-coated steel. The reduction from the uncoated to DC condition is approximately 80.3%, although quantitative comparability also depends on sampling volume, exposure area, analytical calibration and replicate uncertainty.

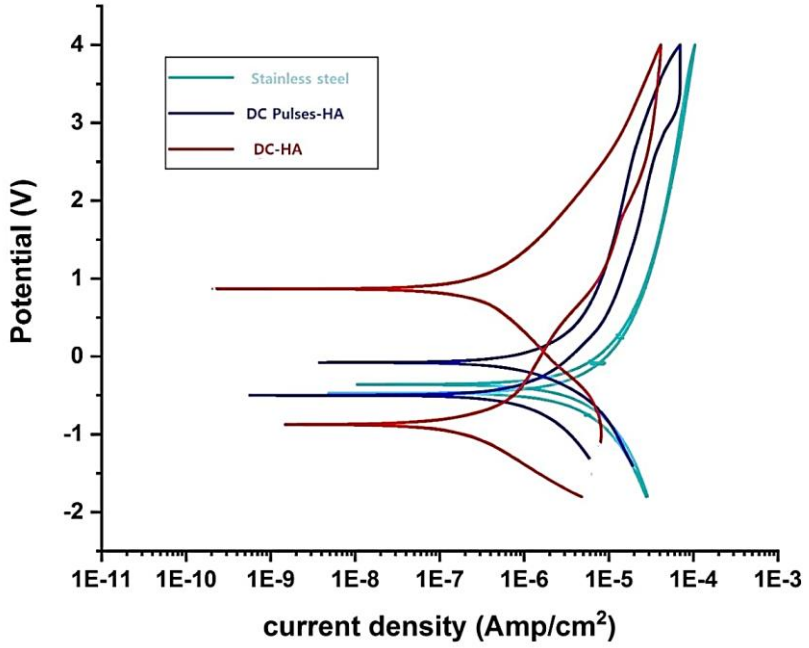

Figure 7. Cyclic polarization curves of (1) Stainless steel (2) DC Pulses-HA (3) DC-HA.

Each specimen measured 1.0 cm in length, 1.0 cm in width, and 0.5 cm in thickness. Only the planar 10 × 10 mm face of each 316L specimen was exposed during polarization (area A = 100 mm² = 1.00 cm²); the 5 mm-thick edges and rear face were masked. Consequently, the recorded total corrosion current Icorr (A) was converted to current density icorr (A/cm²) by division by 1.00 cm². Corrosion penetration-rate

ACCEPTED MANUSCRIPT

estimates were calculated using CR (mm/year) = 0.00327 × icorr (μA/cm²) × EW (g/equiv)/ρ (g/cm³), with assumed 316L EW = 25.5 g/equiv and ρ = 8.00 g/cm³. These are uniform-penetration approximations based on Faraday's law, not directly measured mass-loss rates; further confidence would require alloy-specific EW and verification of Tafel fits.

3.7 Electrochemical behaviors

Corrosion-potential, current-density, open-circuit and Tafel parameters are summarized in Table 9. Recalculated values use the same single-face exposed area for all three samples, ensuring an area-normalized comparison. The rates should not be combined with earlier unnormalized current values or incompatible rate estimates; and localized attack cannot be excluded using a uniform-rate parameter.

Table 9. Electrochemical corrosion parameters and pitting tendency of the investigated samples.

Sample Type	Ecorr (V)	Icorr (A)	icorr (A/cm²)	Corr. Rate (mm/year)	βc	βa	OCP (V)
Stainless steel	-0.677	1.865×10^{-5}	1.8650×10^{-5}	0.194391	0.228	0.171	-0.531
DC Pulses-HA	-0.580	6.190×10^{-7}	6.1900×10^{-7}	0.006452	0.196	0.207	-0.518
DC-HA	-0.389	1.111×10^{-7}	1.1110×10^{-7}	0.001158	0.303	0.175	-0.103

The electrochemical corrosion behavior of uncoated 316L stainless steel and hydroxyapatite-coated samples prepared using direct current (DC) and pulsed direct current (PDC) was evaluated through corrosion potential (Ecorr), corrosion current (Icorr), corrosion current density (icorr), corrosion penetration rate, open-circuit potential (OCP), and anodic and cathodic Tafel slopes (βa and βc), as presented in Table 9. The

ACCEPTED MANUSCRIPT

results demonstrate that both coating techniques substantially improved the electrochemical corrosion resistance of 316L stainless steel, with the DC-HA coating exhibiting the highest protection under the investigated experimental conditions.

The uncoated stainless steel exhibited the highest corrosion current density of 1.8650×10^{-5} A/cm², corresponding to a corrosion current of 1.865×10^{-5} A, based on an exposed surface area of 1.00 cm². Its corrosion potential and open-circuit potential were -0.677 V and −0.531 V, respectively, while the calculated corrosion rate reached 0.194391 mm/year. These results indicate that the uncoated surface was more susceptible to electrochemical corrosion than the coated specimens. The comparatively high current density reflects greater electrochemical activity at the exposed steel–electrolyte interface.

Following the application of the PDC-HA coating, the corrosion current density decreased significantly to 6.1900×10^{-7} A/cm², corresponding to a corrosion current of 6.190×10^{-7} A. The corrosion rate was reduced to 0.006452 mm/year, representing an approximately 96.68% reduction in corrosion current density and 96.68% reduction in corrosion rate relative to uncoated stainless steel. Moreover, Ecorr shifted positively from -0.677 V to -0.580 V, while OCP increased slightly from -0.531 V to -0.518 V. These changes indicate improved electrochemical stability, which can be attributed to the protective action of the deposited HA coating in reducing the effective interaction between the stainless-steel substrate and the corrosive electrolyte.

The DC-HA-coated sample demonstrated the most favorable corrosion behavior among the investigated specimens. Its corrosion current density decreased to 1.1110×10^{-7} A/cm², corresponding to a corrosion current of 1.111×10^{-7} A. Furthermore, the corrosion rate reached the lowest recorded value of 0.001158 mm/year, representing

ACCEPTED MANUSCRIPT

approximately 99.40% improvement in corrosion resistance based on corrosion current density and corrosion rate compared with uncoated stainless steel. The corrosion potential shifted to -0.389 V, indicating a positive displacement of 0.288 V relative to the uncoated substrate. Additionally, OCP increased considerably to -0.103 V, suggesting a more noble electrochemical surface condition.

A direct comparison between the two coating techniques revealed that the DC-HA coating reduced corrosion current density by approximately 82.05% relative to PDC-HA, with a corresponding reduction of approximately 82.05% in the calculated corrosion rate. The DC-HA coating also exhibited a more positive corrosion potential by 0.191 V and a more positive OCP by 0.415 V compared with PDC-HA. These findings suggest that the DC deposition conditions produced a more effective electrochemical barrier under the investigated conditions. Such improvement may be associated with differences in coating continuity, surface coverage, and defect distribution, although the electrochemical measurements alone cannot independently confirm these structural characteristics.

The anodic and cathodic Tafel slopes further illustrate differences in the electrochemical responses of the investigated surfaces. The uncoated stainless steel exhibited $\beta a = 0.171$ and $\beta c = 0.228$, whereas the PDC-HA coating showed $\beta a = 0.207$ and $\beta c = 0.196$. In contrast, DC-HA exhibited $\beta a = 0.175$ and $\beta c = 0.303$. These variations suggest that the deposited coatings modified the anodic dissolution and cathodic reaction kinetics at the electrode–electrolyte interface. In particular, the greater cathodic Tafel slope observed for DC-HA indicates a change in the potential dependence of the cathodic reaction. However, individual Tafel slopes do not provide sufficient evidence to identify a specific corrosion reaction mechanism without additional kinetic characterization.

Accepted Manuscript

ACCEPTED MANUSCRIPT

The corrosion penetration rates presented in Table 9 were evaluated using the conventional relationship between corrosion current density, equivalent weight, and material density, assuming an equivalent weight of 25.5 g/equiv and a density of 8.00 g/cm³ for 316L stainless steel. Under these assumptions, the coated specimens exhibited substantially lower estimated uniform corrosion rates than the uncoated substrate. The use of the same exposed surface area of 1.00 cm² for all specimens also ensures that relative reductions in total corrosion current and area-normalized corrosion current density are equivalent.

Although the positive shifts in Ecorr and OCP, together with the substantial reductions in corrosion current density, demonstrate improved general electrochemical corrosion resistance, these parameters do not independently establish complete resistance to localized pitting. The available polarization data are therefore interpreted primarily in terms of relative corrosion kinetics and barrier performance rather than definitive pitting suppression. Overall, the electrochemical findings establish the following order of corrosion resistance under the investigated conditions:

DC-HA>PDC-HA>Uncoated 316L

The DC-HA coating achieved the lowest corrosion current density (1.1110×10^{-7} A/cm²), the lowest calculated corrosion rate (0.001158 mm/year), and the most positive Ecorr (-0.389 V) and OCP (-0.103 V). These results demonstrate that DC deposition was more effective than PDC deposition in improving the measured electrochemical corrosion resistance of HA-coated 316L stainless steel under the present experimental conditions.

ACCEPTED MANUSCRIPT

Table 10. Percentage reductions in corrosion current density and corrosion rate for DC- and PDC-deposited hydroxyapatite coatings on 316L stainless steel.

Comparison item	Value
Reduction in Icorr for DC Pulses-HA compared with stainless steel	96.68%
Reduction in Icorr for DC-HA compared with stainless steel	99.40%
Reduction in Icorr for DC-HA compared with DC Pulses-HA	82.05%
Reduction in corrosion rate for DC Pulses-HA compared with stainless steel	96.68%
Reduction in corrosion rate for DC-HA compared with stainless steel	99.40%
Reduction in corrosion rate for DC-HA compared with DC Pulses-HA	82.05%

The electrochemical comparison demonstrates a reduced apparent corrosion current density after coating, with the lowest value measured for the DC–HA–chitosan surface (1.1110×10^{-7} A/cm²). Its estimated uniform corrosion rate under the stated EW and density assumptions is 0.001158 mm/year, compared with 0.194391 mm/year for bare steel. This calculated protection does not independently establish freedom from pitting or long-term in-vivo compatibility.

4. Conclusion

The results support deposition of HA–chitosan composites on 316L by both DC and PDC electrophoretic routes, with measured differences in thickness, apparent porosity, cross-cut retention and area-normalized electrochemical behavior. The strongest directly observed thickness in the DC L9 series was 23.25 µm at 60 V, 6 min, nominal HA level 3 and Ra 0.05 µm. The previously reported 23.45 µm confirmation thickness has not been reconciled with a clearly documented confirmation protocol. The single-face electrochemical measurements show that DC-coated material provided the lowest corrosion current density, approximately 99.40% lower than uncoated steel.

The DC coating showed 6.8% affected cross-cut area (approximately ASTM D3359 class

ACCEPTED MANUSCRIPT

3B), compared with 17% (approximately class 2B) for PDC. The corresponding modeled uniform penetration rates were approximately 0.001158 and 0.006452 mm/year, versus 0.194391 mm/year for bare 316L, subject to the stated area and alloy-property assumptions. These findings identify DC deposition as preferable within the tested dataset. The results should be understood as laboratory structural and corrosion indicators rather than evidence for validated long-term implantation, absolute freedom from pitting, or quantitative adhesive bond strength.

References

1. Azar V, Hashemi B, Yazdi MR. The effect of shot peening on fatigue and corrosion behavior of 316L stainless steel in Ringer's solution. Surf Coat Technol. 2010; 15:204(21):3546-3551. https://doi.org/10.1016/j.surfcoat.2010.04.015.
2. Gopi D, Ramya S, Rajeswari D, Kavitha L. Corrosion protection performance of porous strontium hydroxyapatite coating on polypyrrole coated 316L stainless steel. Colloid Surf B: Biointerf. 2013; 1(107):130-136. https://doi.org/10.1016/j.colsurfb.2013.01.065.
3. Radhi MA, Mustafa AM, Abdulkareem MH. Corrosion behavior of nano bio coating on AZ31 magnesium alloy by electrophoretic deposition for biomedical application. Adv Sci Technol Res J. 2025; 19(8) :296-312. https://doi.org/10.12913/22998624/205765.
4. Avcu E, Baştan FE, Abdullah HZ, Rehman MAU, Avcu YY, Boccaccini AR. Electrophoretic deposition of chitosan-based composite coatings for biomedical applications: A review. Prog Mater Sci. 2019; 103:69-108.

ACCEPTED MANUSCRIPT

https://doi.org/10.1016/j.pmatsci.2019.01.001.

5. Zhitomirsky D, Roether JA, Boccaccini AR, Zhitomirsky I. Electrophoretic deposition of bioactive glass/polymer composite coatings with and without HA nanoparticle inclusions for biomedical applications. J Mater Proc Technol. 2009; 19;209(4):1853-1860. https://doi.org/10.1016/j.jmatprotec.2008.04.034.
6. Djošić M, Janković A, Mišković-Stanković V. Electrophoretic deposition of biocompatible and bioactive hydroxyapatite-based coatings on titanium. Materials. 2021; 18;14(18):5391. https://doi.org/10.3390/ma14185391.
7. Han X, Yang D, Yang C, Spintzyk S, Scheideler L, Li P, et al. Carbon fiber reinforced PEEK composites based on 3D-printing technology for orthopedic and dental applications. J Clinical Med. 2019; 12;8(2):240. https://doi.org/10.3390/jcm8020240.
8. Almasi D, Iqbal N, Sadeghi M, Sudin I, Abdul Kadir MR, Kamarul T. Preparation methods for improving PEEK's bioactivity for orthopedic and dental application: a review. Inter J Biomater. 2016; 2016(1):8202653. https://doi.org/10.1155/2016/8202653.
9. Abbas AS, Mahdi BS, Abbas HH, Sayyid FF, Mustafa AM, Annon IA, et al. Corrosion behavior optimization by nanocoating layer for low carbon steel in acid and salt media. Corr Scien Technol. 2023; 22(1):1-9. https://doi.org/10.14773/cst.2023.22.1.1.
10. Zhang G, Liao H, Li H, Mateus C, Bordes JM, Coddet C. On dry sliding friction and wear behaviour of PEEK and PEEK/SiC-composite coatings. Wear. 2006; 10;260(6):594-600. https://doi.org/10.1016/j.wear.2005.03.017.

Accepted Manuscript

ACCEPTED MANUSCRIPT

11. Hussein MB, Mustafa AM, Abdulkareem MH. A Comparative study on dip coating and corrosion behavior of Ti-13Zr-13Nb and commercially pure titanium alloys coated with YSZ by taguchi design. Salud, Ciencia y Tecnología-Serie de Conferencias. 2024; 3:847. https://doi.org/10.56294/sctconf2024847.
12. Ma J, Wang C, Liang CH. Colloidal and electrophoretic behavior of polymer particulates in suspension. Mater Sci Eng C. 2007; 16;27(4):886-9. https://doi.org/10.1016/j.msec.2006.10.005.
13. Abdulhasan AA, Sheng EL, Mustafa AM, Isa MB. Recent advancements in biocompatible coatings for metallic and non-metallic biomaterials: a review. Corr Sci Technol. 2024; 23(5):449-69. https://doi.org/10.14773/cst.2024.23.5.449.
14. Abtan NS, Sultan AE, Sayyid FF, Alamiery AA, Jaaz AH, Gaaz TS, et al. Enhancing corrosion resistance of mild steel in hydrochloric acid solution using 4-phenyl-1-(phenylsulfonyl)-3-thiosemicarbazide: A comprehensive study. Int J Corros Scale Inhib. 2024; 13(1):435-59. https://doi.org/10.17675/2305-6894-2024-13-1-22.
15. Hussein MB, Abdulkareem MH, Mustafa AM. A study evaluating the improvement of the corrosion properties of a Yttria-stabilized zirconia coated on Ti-alloy by using a Taguchi design. AIP Conf Proc. 2024; 3229(1):070014. https://doi.org/10.1063/5.0236016
16. Mahmoodi S, Sorkhi L, Farrokhi-Rad M, Shahrabi T. Electrophoretic deposition of hydroxyapatite–chitosan nanocomposite coatings in different alcohols. Surf Coat Technol. 2013; 216:106-114. https://doi.org/10.1016/j.surfcoat.2012.11.032.
17. Mohammed HK, Abbas AS, Mustafa AM. Characteristics and properties of bright nickel plated on aluminum substrate type AA - 1100. AIP Conf Proc. 2024;

ACCEPTED MANUSCRIPT

3002(1):080030. https://doi.org/10.1063/5.0206370.

18. Jasim AN, Mohammed A, Mustafa AM, Sayyid FF, Aljibori HS, Al-Azzawi WK, et al. Corrosion inhibition of mild steel in HCl solution by 2-acetylpyrazine: weight loss and DFT studies on immersion time and temperature effects. Prog Color Colorant Coat. 2024;1;17(4):333-350. https://doi.org/10.30509/pccc.2024.167231.1261.
19. Hussein MB, Mustafa AM, Abdulkareem MH, Alamiery A. Comparative corrosion performance of YSZ-coated Ti-13Zr-13Nb alloy and commercially pure titanium in orthopedic implants. South African J Chem Eng. 2024; 1;48(1):40-54. https://doi.org/10.1016/j.sajce.2024.01.005.
20. Abed AK, Mustafa AM, Resen AM. Assessment corrosion and bioactive behavior of bioglass coating on Co-Cr-Mo alloy by electrophoretic deposition for biomedical applications. Corr Sci Technol. 2024; 23(3):179-194. https://doi.org/10.14773/cst.2024.23.3.179.
21. Kwok CT, Wong PK, Cheng FT, Man HC. Characterization and corrosion behavior of hydroxyapatite coatings on Ti6Al4V fabricated by electrophoretic deposition. Appl Surf Sci. 2009; 15;255(13):6736-6744. https://doi.org/10.1016/j.apsusc.2009.02.086.

Accepted Manuscript